RSC
Sustainability

PAPER

View Article Online
View Journal | View Issue

Cite this: *RSC Sustainability*, 2024, **2**, 3490

Received 8th July 2024
Accepted 30th September 2024

DOI: 10.1039/d4su00365a

rsc.li/rscsus

The effect of catalyst precursors on the mechanism of iron-catalysed graphitization of cellulose†

Emily C. Hayward, *[a] Glen J. Smales,[b] Brian R. Pauw,[b] Masaki Takeguchi,[c] Alexander Kulak,[d] Robert D. Hunter[e] and Zoe Schnepp[a]

Iron-catalysed graphitization of biomass is a simple and sustainable route to carbons with high graphitic content. It uses abundant precursors and moderate processing temperatures and generates carbons with high porosity. Recently, it has been demonstrated that the choice of biomass precursor can have a significant impact on the textural and compositional properties of the resulting carbon. In this paper, we demonstrate that the choice of catalyst is also critical to the carbon structure. Aqueous iron(III) nitrate and iron(III) chloride convert cellulose to carbons with very different textural properties. This is due to the choice of iron catalyst changing the mechanism of cellulose decomposition and also the nature of the active graphitization catalyst.

Sustainability spotlight

Clean energy depends on many technologies that use carbons. This includes electrode materials for lithium and sodium batteries and electrocatalyst supports. An exciting route to carbons with high graphitic content is iron-catalysed graphitization, which uses simple iron salts to convert biomass to carbon at moderate temperatures. Numerous authors have employed iron and biomass to generate carbons, but the wide range of precursors and conditions hinders understanding of how to tune the properties of the carbons. This paper presents a comparative study of how different iron salts can have a dramatic effect on the textural properties of carbonized cellulose. Such understanding is essential for investigation and scale-up of iron-catalysed graphitization as a technology.

Introduction

Carbon materials have a broad range of applications including lithium and sodium ion batteries,[1,2] adsorbents for water remediation[3] and supercapacitors.[4] Many of these applications require a balance of properties including porosity, surface area, conductivity and the presence of graphitic or graphene-like features. Biomass is a particularly attractive precursor to carbon materials, due to the diversity of sources and potential valorisation of agricultural and forestry waste streams.[5] Many different types of biomass have been investigated for carbon production, including raw lignocellulosic biomass[6,7] and biomass extracts such as cellulose[8] or glucose.[9] These can be converted to carbons *via* pyrolysis,[10] catalytic graphitization[11] or hydrothermal carbonization.[12] One of the most important factors for widespread application of carbons from biomass is the ability to reliably tune the structure and properties. While the effects of processing parameters on pyrolysis[13,14] and hydrothermal carbonization[15] have been studied in detail, catalytic graphitization has received a lot less attention.

Catalytic graphitization is the use of metal catalysts to produce graphitic carbons at moderate temperatures. Biomass is combined with a metal-containing compound and heated in an inert atmosphere to temperatures above 700 °C. Metal nanoparticles are generated *in situ* and catalyse the conversion of biomass-derived amorphous carbon to graphitic nanostructures such as nanotubes.[7] The impact of biomass type on the structure and properties of carbons produced by catalytic graphitization is now quite well understood.[3,16,17] However, the influence of different graphitization catalysts has received a lot less attention. Across the literature, the numerous examples of catalytic graphitization use a wide range of catalyst precursors, including chloride, nitrate, citrate and acetate salts of iron, cobalt, and nickel, or metal/metal oxide nanoparticles. This makes it very difficult to make general conclusions about how different precursors impact the properties of the resulting carbon.

In this paper, we investigate of the effect of different iron salt catalysts on the mechanism of graphitization of cellulose. Cellulose is one of the most promising biomass precursors for graphitization, as it is the most abundant biopolymer on the

---

[a] *School of Chemistry, University of Birmingham, B15 2TT, UK. E-mail: ech620@bham.ac.uk*
[b] *Bundesanstalt für Materialforschung und -prüfung (BAM), Unter den Eichen 87, Berlin 12205, Germany*
[c] *Center for Basic Research on Materials, National Institute for Materials Science, 1-2-1 Sengen, Tsukuba, Ibaraki, 305-0047, Japan*
[d] *School of Chemistry, University of Leeds, Leeds, LS2 9JT, UK*
[e] *Department of Chemical Engineering, Imperial College London, London SW7 2AZ, UK*

† Electronic supplementary information (ESI) available. See DOI: https://doi.org/10.1039/d4su00365a

planet, with 1.5 × 10^{12} tons produced in nature each year.[18] It can be extracted readily and on a very large scale from wood and agricultural waste, making it ideal as a sustainable precursor for materials and as a subject for this study. Previous reports on graphitization of cellulose have used nickel, cobalt and iron salts and shown that it is possible to generate carbons with graphitic nanostructures such as hollow graphitic shells,[19] ribbon-like morphologies[20,21] or multi-walled graphitic carbon nanotubes.[19] It is also apparent that different iron salts can impact carbon structure. For example, cellulose spheres treated with iron nitrate produced carbons with a mixture of micro- and mesoporosity, whereas iron chloride produced highly microporous carbons.[20] The authors suggested that the higher Lewis acidity of iron chloride was responsible for the different structures but the mechanism of cellulose decomposition with different iron salts was not studied. In this paper, we demonstrate that different iron salts change the structure and properties of cellulose-derived carbons by changing the cellulose decomposition mechanism and the size distribution of the graphitization catalyst. This detailed mechanistic and processing insight is critical if cellulose graphitization is to provide a real option for sustainable carbons.

Results and discussion

Characteristics of graphitic carbon

Carbons were produced by combining microcrystalline cellulose (MCC) with aqueous $Fe(NO_3)_3$ or $FeCl_3$ and heating to 800 °C under nitrogen for 1 h. Powder X-ray diffraction (p-XRD) patterns show a sharp peak at 26.1° for both samples, characteristic of the interplanar spacing of graphitic carbon (Fig. 1a). This synthesis is highly reproducible, with separate samples producing very similar p-XRD patterns when heated under the same conditions (Fig. S1†).[16,17] In contrast, a control sample of cellulose with no catalyst shows only two very broad peaks at 23.5° and 43.6°, indicative of amorphous carbon with some local stacking but no long-range order. Nitrogen porosimetry data of the two iron-catalysed cellulose samples show type IV isotherms indicating a porous structure consisting of both mesopores and micropores (Fig. 1b). In contrast, the control sample shows a type I isotherm, indicating a microporous structure. More detailed information on the surface area and pore volume is provided in Table 1.[22] The presence of mesopores is consistent with the formation of graphitic structures such as shells[23] and nanotubes,[7] which have been observed in previous reports of iron-catalysed graphitization. These shells and nanotubes are formed by catalyst nanoparticles dissolving amorphous carbon and reprecipitating hollow graphitic nanostructures. The nanotube diameter is dependent on the size of the nanoparticle catalyst and nanoparticles within the 10–50 nm size range thus produce mesoporous carbons. Interestingly, the carbon produced from cellulose and $FeCl_3$ contains macropores, as indicated by the continuing adsorption at $p/p_0 = 1$ in the isotherm. This suggests that the catalyst particles are larger in the sample synthesized with $FeCl_3$ than the one synthesized with $Fe(NO_3)_3$. The BET surface area is lower for both graphitized samples, presumably as the microporous amorphous carbon is converted to mesoporous graphitic nanostructures.

Raman microscopy was used to further investigate the nature of the graphitic carbon in each sample. Fig. 2 shows two prominent peaks at 1325 cm^{-1} and 1600 cm^{-1}, corresponding to the D and G peaks respectively. In perfect graphite, only the G peak is allowed (at ∼1581 cm^{-1}) and the D peak is forbidden. Therefore, the presence of the D peak and the deviation of the G peak from the position of perfect graphite indicates that all three cellulose-derived carbons exhibit disorder. To extract peak position and full width half maximum (FWHM) values, a 4 peak Voigt function was used, where peaks are attributed to the G, D1, D3 and D4 bands. The information acquired from this method is detailed in Table 2. The position of the G peak is confirmed to be shifted to higher wavenumber for all three samples, which is consistent with nanocrystalline domains. The ratio of the intensity of the D peak to the G peak (I_D/I_G) is commonly used to provide information on the level of graphitization. However, in this case, there is little difference between values of any of the carbon structures, likely owing to its sensitivity to other factors, such as surface defects. However, the ratio of intensity for the D3 peak compared to that of the G peak (I_{D3}/I_G) has been shown as a good indicator for the ratio of

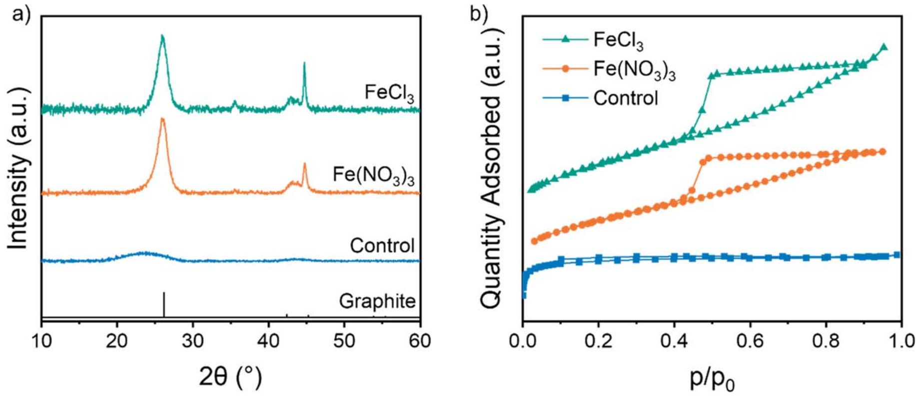

Fig. 1 (a) p-XRD pattern (CuK$_\alpha$ source) and (b) vertically offset N_2 adsorption isotherms of microcrystalline cellulose heated to 800 °C without pre-treatment, or treatment with aqueous $Fe(NO_3)_3$ or $FeCl_3$.

Table 1 Adsorptive properties of carbons produced from microcrystalline cellulose using no additive, $Fe(NO_3)_3$ or $FeCl_3$ and pyrolyzed at 800 °C

Iron salt	Specific surface area ($m^2\ g^{-1}$)	Total pore volume ($cm^3\ g^{-1}$)	Micropore volume ($cm^2\ g^{-1}$)	% Micropores
None	470	0.19	0.16	86
$Fe(NO_3)_3$	360	0.24	0.077	32
$FeCl_3$	370	0.30	0.086	34

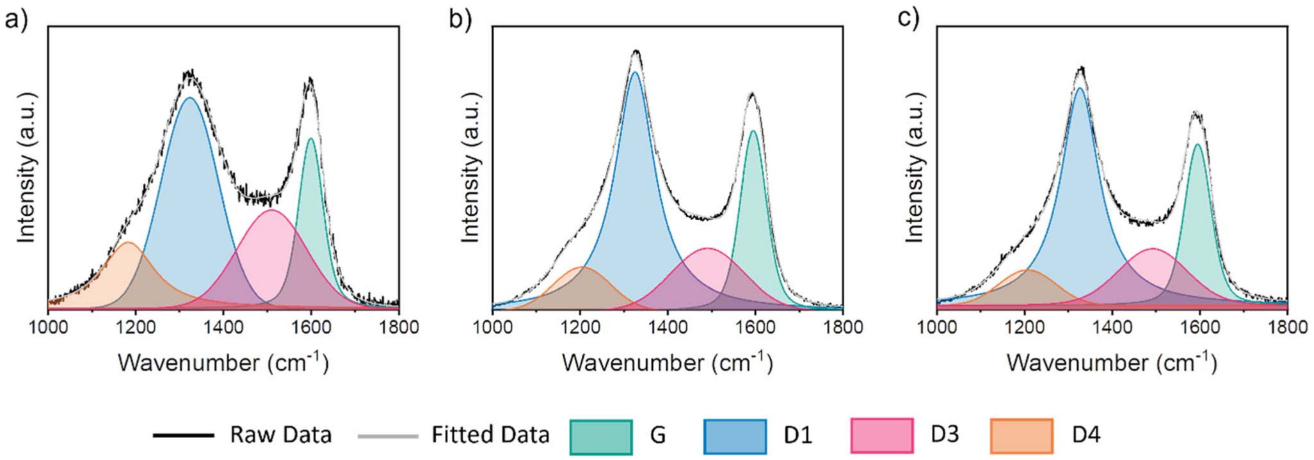

Fig. 2 Raman spectra for microcrystalline cellulose treated with (a) no iron salt, (b) $Fe(NO_3)_3$ and (c) $FeCl_3$ and held at 800 °C for 1 h – including the deconvoluted Raman spectra, fitted using a 4-point Voigt function.

Table 2 Information derived from Raman microscopy after fitting, including G peak position, full width half maximum (FWHM) of G peak, and the intensity ratios of the D and G (I_D/I_G) peaks and the D3 and G peaks (I_{D3}/I_G)

Iron salt	G peak position (cm^{-1})	G peak FWHM (cm^{-1})	I_D/I_G	I_{D3}/I_G
None	1599 ± 1	66.6 ± 3	2.55	1.03
$Fe(NO_3)_3$	1595 ± 1	72.2 ± 2	2.50	0.43
$FeCl_3$	1595 ± 1	72.6 ± 1	2.60	0.40

amorphous to graphitic carbon.[24] Considering these ratios, it is clear that iron catalysts significantly increase graphitic content, but there is little difference between the two iron salts. Given the small differences between the Raman data for the two iron-containing samples, we elected not to analyse the different peak ratios any further.

To investigate the reason for the different textural properties of carbons produced from different iron salts, we used thermogravimetric analysis coupled with mass spectrometry (TGA-MS) to probe the reaction mechanism. For all samples, the TGA data (Fig. 3a) show a single large mass loss between 300 °C and 400 °C, corresponding to thermal decomposition of the cellulose polymer. The onset of mass loss and peak mass loss is at a lower temperature for both the iron-containing samples. The differential thermogravimetric (DTG) data for the $FeCl_3$-containing sample (Fig. 3b) also shows a shoulder at 230–280 °C. This correlates to a peak for $m/z = 18$ in the MS data (Fig. 3c), indicating loss of water. Cellulose pyrolysis involves multiple chemical reactions, including dehydration, depolymerization and ring opening.[25] Char formation can occur *via* direct carbonization of the cellulose or by secondary polymerization of volatile decomposition products.[26] Catalysts such as metal salts are known to influence cellulose decomposition and the DTG data suggest that $FeCl_3$ promotes dehydration reactions at a lower temperature than $Fe(NO_3)_3$.[27] This is consistent with the ability of $FeCl_3$ to act as a Lewis acid and suppress the formation of levoglucosan (Fig. 3f) by promoting dehydration in cellulose, in addition to depolymerisation of the biopolymer.[28–31] Further evidence for this comes from MS data for $m/z = 60$, the most prominent fragment for levoglucosan (Fig. 3d). Both iron salts drive formation of levoglucosan at lower temperatures than pure cellulose and in smaller amounts, but the peak for the cellulose–$FeCl_3$ system is particularly small. The release of CO and CO_2 are more challenging to track as CO is masked by the N_2 atmosphere of the experiment ($m/z = 28$) and CO_2 is overlaid by N_2O ($m/z = 44$). The sharp peak for $m/z = 44$ for the cellulose–$Fe(NO_3)_3$ sample (Fig. 3e) is likely to be a mixture of N_2O and CO_2 as the highly oxidizing nitrate reacts with the cellulose. CO_2 release from the $FeCl_3$–cellulose system starts earlier than for the cellulose control and the peak is smaller. This provides further evidence that the $FeCl_3$ is changing the decomposition reactions significantly. Regardless of the gases released, the yield of the carbon produced using $FeCl_3$ (16%) is higher than that produced using $Fe(NO_3)_3$ (11%). Identical Fe:cellulose molar ratios were used so this indicates that the $FeCl_3$ is promoting cellulose decomposition pathways that lower the

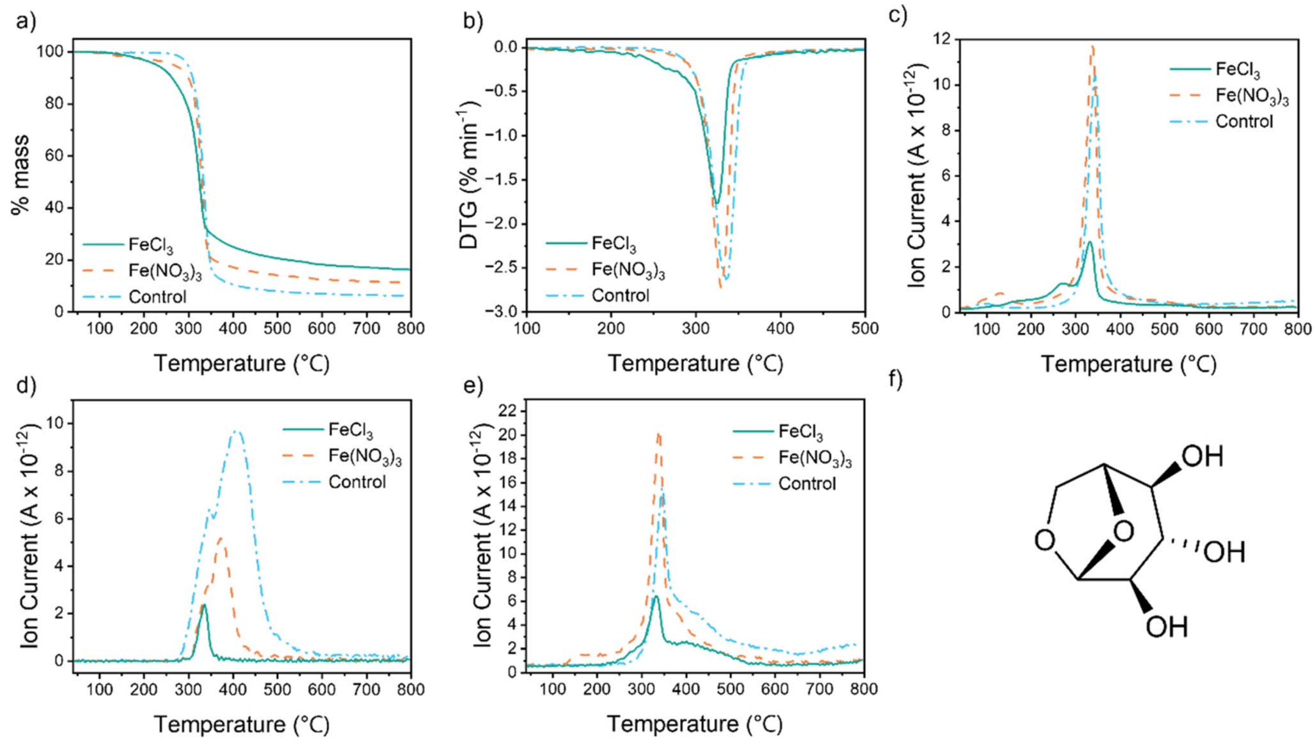

Fig. 3 (a) TGA and (b) DTG data for cellulose, $Fe(NO_3)_3$–cellulose and $FeCl_3$–cellulose pyrolysis in N_2, mass spectrometry data showing temperature-dependent release of ion fragments of m/z = (c) 18, (d) 60 and (e) 44 and (f) structure of levoglucosan.

amount of carbon lost as CO/CO_2 and other volatiles like levoglucosan. This in turn will affect the evolution of pores in the carbon.

Further evidence for the early dehydration of cellulose in the presence of $FeCl_3$ comes from p-XRD data. For raw cellulose and cellulose with $Fe(NO_3)_3$, the characteristic peaks for the cellulose structure (Fig. S2a†) can be seen clearly even after heating to 300 °C (Fig. 4a and b), whereas the peaks disappear between 250 °C and 300 °C for cellulose with $FeCl_3$ (Fig. 4c). The crystal structure of cellulose involves a lot of intra and intermolecular hydrogen bonds, which are broken during dehydration.[32] Therefore the loss of peaks below 300 °C for the cellulose–$FeCl_3$ system is consistent with early onset of dehydration catalysed by the $FeCl_3$. It should be noted that no crystalline iron phases are observable in the p-XRD data up to 400 °C. Investigations of related systems have shown that very small amorphous iron–oxygen clusters or iron oxide nanoparticles evolve during heating of biomass with iron salts so it is possible that similar structures exist alongside the decomposing cellulose but can't be detected by p-XRD.[33]

Fourier transform infrared spectroscopy (FTIR) offers more insight into the molecular transformations involved in the decomposition of cellulose in the three systems. The FTIR spectrum for the control (no iron) sample up to 300 °C (Fig. 4d) shows peaks corresponding to –OH, C–O (ether) and C–O (pyranose), which are all present in the cellulose structure (Fig. S2b†). Most of the peaks disappear by 400 °C, in line with the major mass loss observed at 300–400 °C in the TGA and the loss of peaks in the p-XRD patterns. In their place, small peaks for C=C and C=O emerge, consistent with the formation of decomposition products like levoglucosenone. For both the iron-containing samples (Fig. 4e and f), there is a significant loss of functionality below 300 °C, as indicated by a decrease in FTIR peak intensity between 250 °C and 300 °C. The OH peak is not present at 300 °C, consistent with dehydration processes. The C–O ether peak also disappears by 300 °C, which suggests a significant amount of depolymerization in both iron-containing systems. Interestingly, for the cellulose–$Fe(NO_3)_3$ system, the C–O pyranose peak disappears completely by 300 °C, suggesting ring opening is one of the decomposition pathways. Iron oxides have been shown to catalyse ring-opening during cellulose decomposition as well as participate in depolymerization and dehydration.[34,35] This could indicate that small iron oxide clusters are formed during pyrolysis of cellulose–$Fe(NO_3)_3$, as has been observed in other biomass–$Fe(NO_3)_3$ systems.[33] For both iron-containing systems, C=C and C=O peaks are observed from 300 °C, again showing how the iron promotes carbonization in these systems.

The later stages of cellulose carbonization were investigated using *ex situ* p-XRD. Fig. 5a shows that carbonization of pure cellulose does not produce any crystalline graphitic carbon, as expected. In contrast, the carbonization of cellulose–$Fe(NO_3)_3$ produces a characteristic peak for graphitic carbon at 26.1° (Fig. 5b). This occurs alongside peaks for Fe_3C and α-Fe, which is consistent with the formation of Fe/Fe_3C catalyst nanoparticles. At 600 °C and 500 °C, there are no peaks in the p-XRD patterns for the cellulose–$Fe(NO_3)_3$ system, suggesting that iron is present as very small nanoparticles or only as amorphous

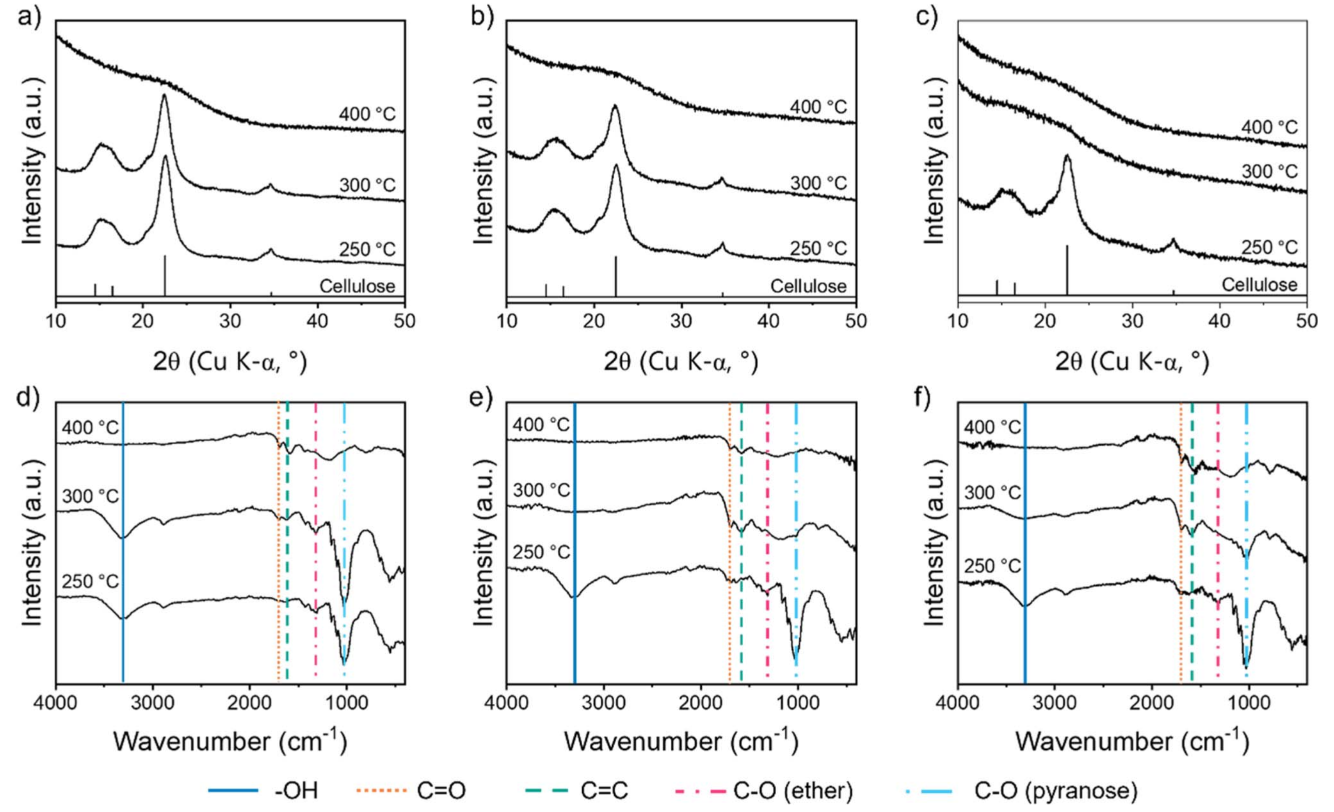

Fig. 4 p-XRD patterns for microcrystalline cellulose treated with (a) no iron salt, (b) $Fe(NO_3)_3$ and (c) $FeCl_3$ and heated to various temperatures. FTIR spectra for microcrystalline cellulose treated with (d) no iron salt, (e) $Fe(NO_3)_3$ and (f) $FeCl_3$, and heated to various temperatures.

clusters. In contrast, the pyrolysis of cellulose with $FeCl_3$ produces sharp peaks for iron oxide (primarily Fe_3O_4) from 500 °C (Fig. 5c). The lack of significant peak broadening indicates the iron oxide particles are relatively large. From 700 °C, the iron oxide peaks have been replaced by sharp peaks for α-Fe with a very small presence of graphitic carbon and by 800 °C the graphitic carbon peak is fully developed with some α-Fe replaced by Fe_3C. The *ex situ* nature of the experiments means that we cannot make conclusions as to the identity of the catalyst in the two systems. However, the data strongly suggests two different routes to reaching the active graphitization catalysts with much larger crystalline species formed in the $FeCl_3$ system. This would be consistent with the observation of macropores in the cellulose–$FeCl_3$-derived carbon.

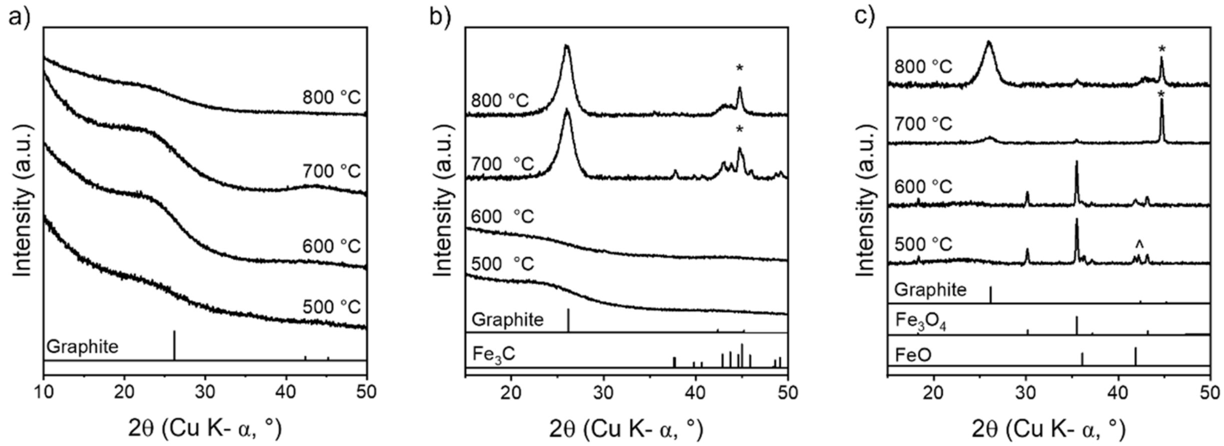

Fig. 5 *Ex situ* p-XRD patterns of microcrystalline cellulose treated with (a) no catalyst, (b) $Fe(NO3)_3$ and (c) $FeCl_3$ and heated to 500 °C, 600 °C, 700 °C and 800 °C for 1 h. Samples are cooled prior to analysis, therefore, any high temperature phases (e.g. γ-Fe) which may be present at high temperature are not seen in the *ex situ* p-XRD patterns. Peaks marked * correspond to a reference pattern for Fe (ferrite) and peaks marked ^ correspond to $Fe_{0.911}O$.

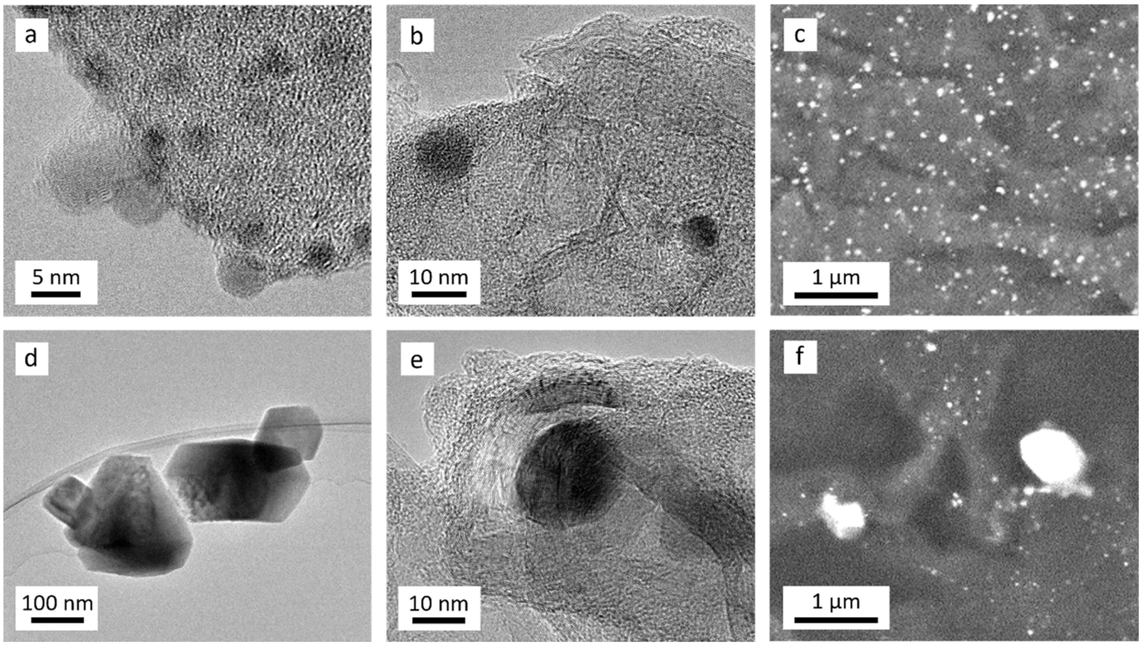

Fig. 6 TEM images of cellulose treated with $Fe(NO_3)_3$ and heated to (a) 600 °C and (b) 700 °C and (c) SEM image of cellulose–$Fe(NO_3)_3$ after heating at 800 °C. TEM images of cellulose treated with $FeCl_3$ and heated to (d) 600 °C and (e) 700 °C and (f) SEM image of cellulose–$FeCl_3$ after heating at 800 °C.

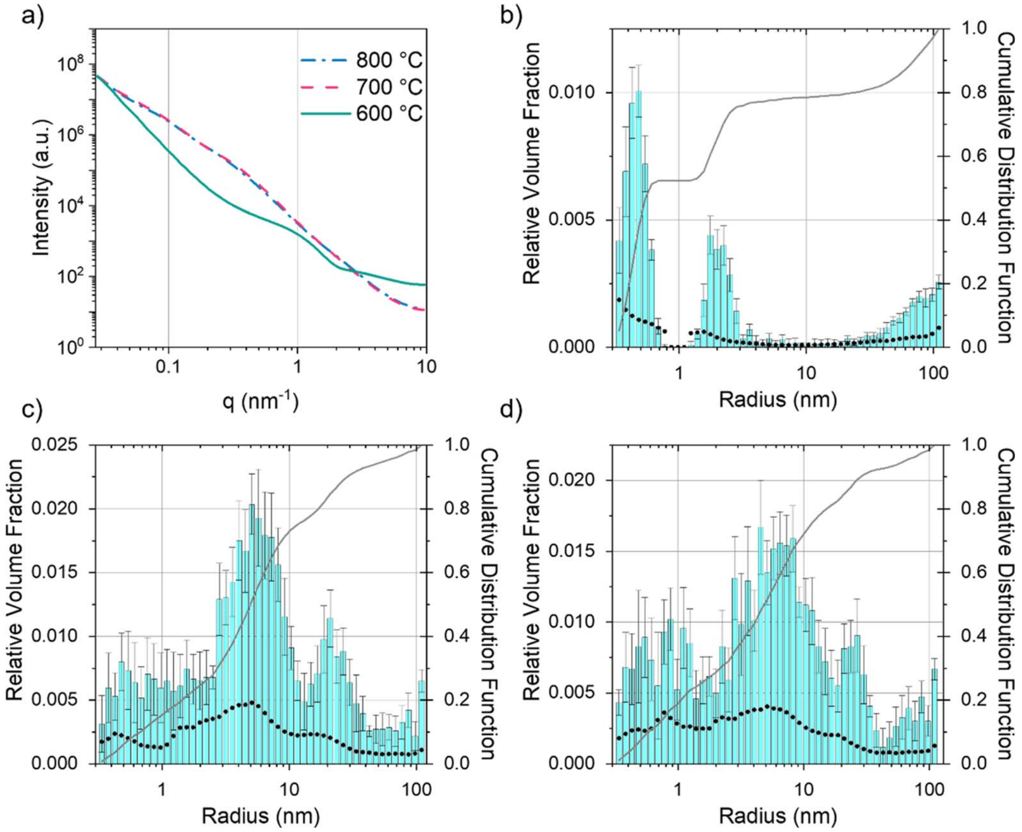

Fig. 7 (a) Fitted SAXS data for microcrystalline cellulose treated with $Fe(NO_3)_3$ and held at 600 °C, 700 °C and 800 °C for 1 h. Particle size histograms coupled with visibility limits (black dots, left *y*-axis) and cumulative distribution functions (right *y*-axis) for microcrystalline cellulose treated with $Fe(NO_3)_3$ and held at (b) 600 °C, (c) 700 °C and (d) 800 °C for 1 h.

Transmission electron microscopy (TEM) was used to further probe the evolution of catalyst particles in the two cellulose–Fe systems. After heating to 600 °C (Fig. 6a), the cellulose–$Fe(NO_3)_3$ sample shows very small (<5 nm in diameter) dark spots of more electron-dense material, indicating iron-rich nanoparticles. No evidence of lattice fringes could be seen, which could indicate that the nanoparticles are amorphous. This is consistent with the lack of peaks in the p-XRD data. The nanoparticles are larger and more clearly defined with increasing temperature (Fig. 6b), consistent with the appearance of Fe_3C/Fe peaks in the p-XRD data. From 700 °C, stacked layers of graphitic carbon can be seen, characteristic of hollow shells and nanotubes formed by catalytic graphitization. Scanning electron microscopy (SEM) with back-scattered electron detector shows the Fe_3C/Fe nanoparticles are small and evenly distributed across the carbon (Fig. 6c, full image included in Fig. S3†). In contrast, the cellulose–$FeCl_3$ sample showed large (>100 nm in diameter), faceted particles after heating to 600 °C, many of which had become detached from the underlying carbon when dispersed on the TEM grid (Fig. 6d). This is consistent with the sharp peaks for Fe_3O_4 in the p-XRD. We propose that the large particles are a result of halide vapour hydrolysis, where volatile $FeCl_3 \cdot 6H_2O$ vaporises and reacts with water evolved during heating. The result is the deposition of large magnetite (Fe_3O_4) particles.[36] In contrast, $Fe(NO_3)_3$ decomposes during heating and so remains spread homogeneously throughout the sample.[37] After heating to 700 °C (Fig. 6e), the $FeCl_3$–cellulose sample appears to be similar to the $Fe(NO_3)_3$–cellulose system, with dark iron-rich particles within layers of graphitic carbon nanostructures. However, the SEM shows that the particles are much more variable in size, with some particles hundreds of nm in diameter (Fig. 6f, full image included in Fig. S4†). This is consistent with porosimetry data, which indicated a mixture of meso- and macroporosity in the carbon produced using $FeCl_3$.

Given that SEM and TEM are microscopic techniques, small angle X-ray scattering (SAXS) was performed on bulk amounts of sample to provide averaged structural information. For carbons prepared from cellulose and $Fe(NO_3)_3$ there is a clear increase in scattering between 600 °C and 700 °C (Fig. 7a). At 600 °C, the broad peak in the scattering data around $q = 1\ \text{nm}^{-1}$ corresponds to scattering features around 5 nm in diameter, consistent with the small particles/clusters observed in TEM images. The data in q range $0.027 \leq q\ (\text{nm}^{-1}) \geq 9.87$ were fitted and analysed using McSAS, a Monte Carlo method to extract form-free size distributions (full details in ESI,† including full range of collected in Fig. S5† and data with fit lines in Fig. S6†).[38] The size histogram for the scattering structures present in the $Fe(NO_3)_3$–cellulose system at 600 °C (Fig. 7b) shows three main features. The peak at very low radius (<1 nm) can be assigned to micropores and surface roughness (caused by scattering from the carbon–air interface). The central peak (between 2–3 nm) is ascribed to the developing iron particles

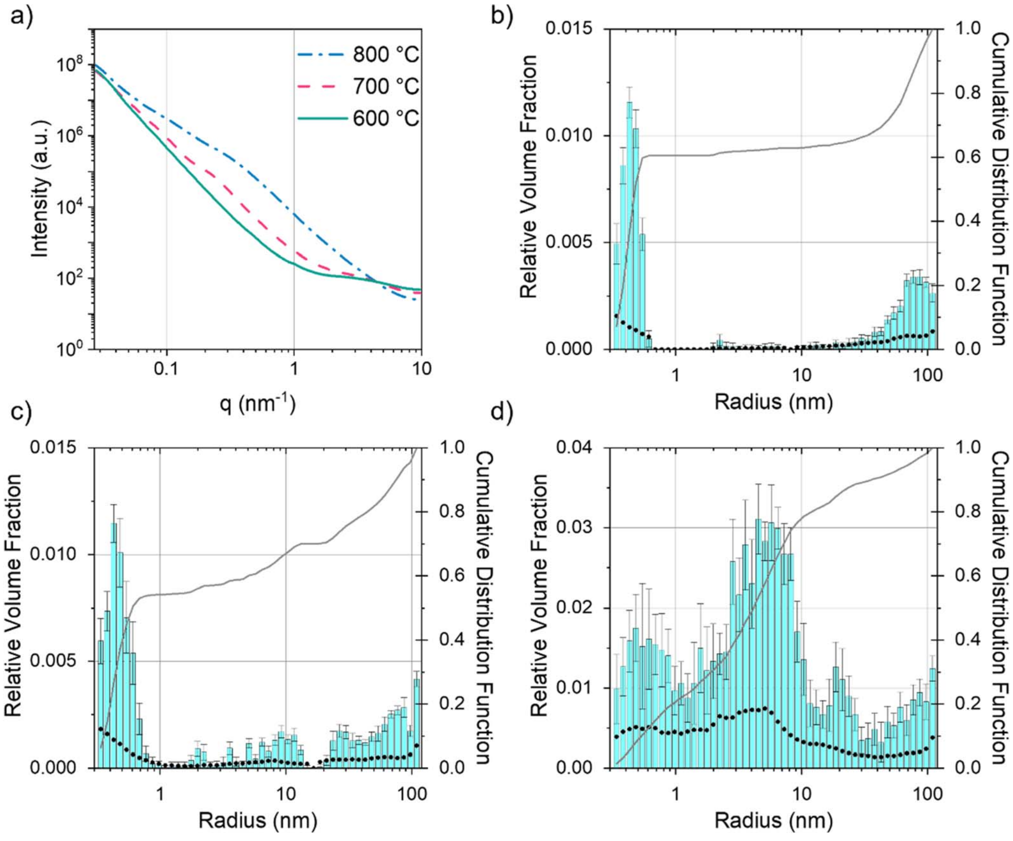

Fig. 8 (a) Fitted SAXS data for microcrystalline cellulose treated with $FeCl_3$ and held at 600 °C, 700 °C and 800 °C for 1 h. Particle size histograms coupled with visibility limits (black dots, left y-axis) and cumulative distribution functions (right y-axis) for microcrystalline cellulose treated with $FeCl_3$ and held at (b) 600 °C, (c) 700 °C and (d) 800 °C for 1 h.

and the features at large radius (>20 nm) are likely caused by larger pores from the original cellulose structure. At 700 °C and 800 °C (Fig. 7c and d), the main contribution to the scattering comes from features in the 3–40 nm size range, consistent with both the catalyst nanoparticles and the mesopores in the graphitic nanostructures. The $FeCl_3$–cellulose system shows a similar increase in scattering from 600 °C to 800 °C (Fig. 8a). However, the broad peak centred around $q = 1\ nm^{-1}$ is not present at 600 °C and there is a corresponding lack of features in the 3–40 nm size range in the histogram (Fig. 8b). This is consistent with TEM, which only showed large, faceted crystals, unlike the small nanoparticles/clusters seen in the $Fe(NO_3)_3$–cellulose system. The large crystals would be well outside of the size range probed by SAXS. At 700 °C, the histogram (Fig. 8c) indicates the emergence of some scattering features around 10 nm in radius, consistent with the observation of nanoparticles in the TEM. At 800 °C, the scattering profile and histogram (Fig. 8d) are both similar to those of the $Fe(NO_3)_3$–cellulose system, again consistent with the observation of nanoparticle catalysts and graphitic nanostructures with mesopores.

Conclusions

This study has comprehensively examined the impact of using $Fe(NO_3)_3$ and $FeCl_3$ as catalysts for the iron-catalysed graphitization of cellulose. The influence of the counterion (NO_3^- or Cl^-) on yield and textural properties is considerable, with $FeCl_3$ promoting a higher yield of carbon with nitrogen porosimetry data providing evidence that porosity extends from micro to macropores. This is in comparison to a primarily mesoporous carbon produced from cellulose with $Fe(NO_3)_3$. The reason for the difference in material properties is that the iron salts promote different decomposition pathways, presumably due to the different Lewis acidity of the salts. Iron chloride promotes dehydration of cellulose and strongly suppresses the formation of levoglucosan, a volatile decomposition product. This in turn means that the iron chloride generates a higher carbon yield than iron nitrate. Another major difference between the two systems is the volatility of $FeCl_3$. Vaporization of the chloride and subsequent hydrolysis results in the deposition of large iron oxide crystallites. These in turn produce large Fe/Fe_3C catalyst particles which generate graphitic macropores. This is in contrast to the $Fe(NO_3)_3$–cellulose system, which remains amorphous until >600 °C, with the iron highly dispersed. The resulting catalyst particles are much smaller, resulting in a mesoporous graphitic structure. Thus, a simple change in metal salt can have a significant impact on material properties in pyrolysis. This is a powerful tool for tuning carbon porosity and structure.

Experimental

Materials

Microcrystalline cellulose (<20 μm), iron nitrate nonahydrate and iron(III) chloride hexahydrate were purchased from Sigma-Aldrich and used without any further modification.

Preparation of cellulose samples with iron salts

In all cases, 0.68 mmol iron salt was dissolved in 40 mL of water at room temperature and added to 20 g of microcrystalline cellulose (MCC). The mixture was stirred manually until the liquid was absorbed and dried in a 70 °C oven overnight. For pyrolysis, 2 g of sample was placed in an alumina crucible and heated to desired temperature (250, 300, 400, 500, 600, 700 and 800 °C) at a rate of 5 °C min^{-1} under N_2 atmosphere with flow rate 1 L min^{-1}. The samples were held at this temperature for 1 h before cooling to room temperature.

Fourier transformed infrared spectroscopy

Infrared spectroscopy was collected using Bruker Alpha FT-IR spectrometer with an ATR attachment.

Thermogravimetric analysis

Thermogravimetric analysis was carried out using Netzsch STA 449 F3 Jupiter and mass spectrometry data collected by QMS 403 Aeolos Quadro. Thermograms were collected with average sample mass between 5–10 mg and heated at 10 °C min^{-1} between 40–800 °C under N_2 atmosphere.

Powder X-ray diffraction

Samples were ground into a fine powder and placed on low-background silicon wafer sample holders. p-XRD experiments were performed using a PANalytical Empyrean diffractometer with a copper anode (wavelengths: $K\alpha1 = 1.5406$ Å, $K\alpha2 = 1.5443$ Å) and a Pixel 2D detector. The diffractometer did not have a monochromator but the Kβ radiation was removed with a nickel filter.

Raman spectroscopy

Samples were ground to a fine powder and placed on a glass slide. Raman spectroscopy was taken using Renishaw inVia Raman microscope using a red laser at 10% power with wavelength of 633 nm. Peak fitting was completed using assuming a 4-peak Voigt function. The 5-peak fit was not used owing to significant overlap between the G and D_2 peaks in the spectra.

Scanning electron microscopy

Samples were mounted on an SEM stub using an adhesive copper tape. Samples were viewed with a FEM-SEM FEI Nova 450 using a CBS detector, operating at 5 kV with deceleration mode.

Small angle X-ray scattering

Samples were ground into a fine powder and distributed across a hole in a paper sample holder between two pieces of Scotch Magic tape. The wide-range SAXS experiments were performed using the Multi-scale Analyser for Ultrafine Structures (MAUS) at the Federal Institute for Materials Research and Testing (BAM), Berlin. Copper and molybdenum anodes (8 eV and 17 eV photons, respectively) were used to measure over a wide q range.

Transmission electron microscopy

Approx. 50 mg of sample was dispersed in approx. 1 mL ethanol and sonicated for around 10 minutes. Subsequently samples were drop cast onto an E-chip for the Protochips FUSION heating holder. Samples were observed using a JEOL JEM-2100F in TEM mode at 200 kV acceleration voltage.

Nitrogen sorption

Nitrogen sorption measurements were carried out using a Quantachrome Nova 1000 series volumetric gas sorption analyser at 77 K. 50–200 mg sample was ground to fine powder and degassed at 100 °C for 24 h under vacuum. Isotherms were carried out with sample tubes calibrated for filler rods over the pressure range p/p_0 0.015–0.095. BET surface areas were calculated using the Rouquerol correction to select range p/p_0 0.015–0.04 using the method recommended by the International Organization for Standardization (ISO) 9277.[39] The total pore volume was obtained from the isotherm plateau and the micropore volume was obtained using the *t*-plot method, according to ISO 15901-2.[40]

Data availability

All data associated with this paper are openly available from **https://doi.org/10.25500/edata.bham.00001143**.

Conflicts of interest

There are no conflicts to declare.

Acknowledgements

The authors acknowledge the Leverhulme Trust (Grant RPG-2020-076) and the University of Birmingham (EH PhD studentship) for funding. This work made use of Aalto University Bioeconomy Facilities.

References

1 H. Zhu, F. Shen, W. Luo, S. Zhu, M. Zhao and B. Natarajan, *Nano Energy*, 2017, **33**, 37–44.
2 M. Drews, J. Büttner, M. Bauer, J. Ahmed, R. Sahu, C. Scheu, S. Vierrath, A. Fischer and D. Biro, *Chemelectrochem*, 2021, **8**, 4750–4761.
3 R. D. Hunter, J. Davies, S. J. A. Hérou, A. Kulak and Z. Schnepp, *Philos. Trans. R. Soc., A*, 2021, **379**, 20200336.
4 S. Herou, P. Schlee, A. B. Jorge, M. Titirici and C. Opin, *Green Sustain. Chem.*, 2018, **9**, 18–24.
5 C. O. Tuck, *Science*, 2012, **337**, 695–699.
6 H. M. Coromina, D. A. Walsh and R. Mokaya, *J. Mater. Chem. A*, 2016, **4**, 280–289.
7 E. Thompson, A. E. Danks, L. Bourgeois and Z. Schnepp, *Green Chem.*, 2015, **17**, 551–556.
8 M. Sevilla and A. B. Fuertes, *Chem. Phys. Lett.*, 2010, **490**, 63–68.
9 M. Sevilla, C. Sanchís, T. Valdés-Solís, E. Morallón and A. B. Fuertes, *Carbon*, 2008, **46**, 931–939.
10 L. Li, C. Fan, B. Zeng and M. Tan, *Mater. Chem. Phys.*, 2020, **242**, 122380.
11 R. D. Hunter, J. Ramírez-Rico and Z. Schnepp, *J. Mater. Chem. A*, 2022, **10**, 4489–4516.
12 B. P. Abbott, R. Abbott, T. D. Abbott, B. P. Abbott, R. Abbott, T. D. Abbott, M. Titirici, S. G. Baird, T. D. Sparks, S. M. Yang, A. Brandt-talbot, O. Hosseini, D. P. Harper, R. M. Parker, S. Vignolini, L. A. Berglund, Y. Li, H. Gao, L. Mao, S. Yu, N. Díez, C. J. Stubbs, J. C. Worch, G. A. Ferrero, M. Sevilla, P. Agota, O. Westhead, C. Roy, I. E. L. Stephens, S. A. Nicolae, S. C. Sarma, R. P. Oates, C. Wang, Z. Li and X. J. Loh, *J. Phys.: Mater.*, 2022, **5**, 032001.
13 T. Kan, V. Strezov and T. J. Evans, *Renewable Sustainable Energy Rev.*, 2016, **57**, 1126–1140.
14 D. V. Suriapparao and R. Tejasvi, *Process Saf. Environ. Prot.*, 2022, **162**, 435–462.
15 G. Ischia and L. Fiori, *Waste Biomass Valorization*, 2021, **12**, 2797–2824.
16 R. D. Hunter, J. L. Rowlandson, G. J. Smales, B. R. Pauw, V. P. Ting, A. Kulak and Z. Schnepp, *Adv. Mater.*, 2020, **1**, 3281–3291.
17 R. D. Hunter, E. C. Hayward, G. J. Smales, A. Kulak, S. G. De and Z. Schnepp, *Adv. Mater.*, 2023, **4**, 2070–2077.
18 D. Klemm, B. Heublein, H. P. Fink and A. Bohn, *Angew. Chem., Int. Ed.*, 2005, **44**, 3358–3393.
19 J. Hoekstra, A. M. Beale, F. Soulimani, M. Versluijs-helder, J. W. Geus and L. W. Jenneskens, *J. Phys. Chem. C*, 2015, **119**, 10653–10661.
20 J. Hoekstra, A. M. Beale, F. Soulimani, M. Versluijs-helder, D. Van De Kleut, J. M. Koelewijn, J. W. Geus and L. W. Jenneskens, *Carbon*, 2016, **107**, 248–260.
21 C. Chen, K. Sun, A. Wang, S. Wang and J. Jiang, *Bioresources*, 2018, **13**, 3165–3176.
22 M. Thommes, K. Kaneko, A. V. Neimark, J. P. Olivier, F. Rodriguez-Reinoso, J. Rouquerol and K. S. W. Sing, *Pure Appl. Chem.*, 2015, **87**, 1051–1069.
23 Z. Schnepp, M. J. Hollamby, M. Tanaka, Y. Matsushita, Y. Xu and Y. Sakka, *Chem. Commun.*, 2014, **50**, 5364–5366.
24 A. C. Ferrari and D. M. Basko, *Nat. Nanotechnol.*, 2013, **8**, 235–246.
25 H. Yang, M. Gong, J. Hu, B. Liu, Y. Chen, J. Xiao, S. Li, Z. Dong and H. Chen, *Energy Fuels*, 2020, **34**, 3412–3421.
26 Y. C. Lin, J. Cho, G. A. Tompsett, P. R. Westmoreland and G. W. Huber, *J. Phys. Chem. C*, 2009, **113**, 20097–20107.
27 F. X. Collard, A. Bensakhria, M. Drobek, G. Volle and J. Blin, *Biomass Bioenergy*, 2015, **80**, 52–62.
28 Z. Xu, Z. Sun, Y. Zhou, W. Chen, T. Zhang, Y. Huang and D. Zhang, *Colloids Surf., A*, 2019, **582**, 123934.
29 N. Shimada, H. Kawamoto and S. Saka, *J. Anal. Appl. Pyrolysis*, 2008, **81**, 80–87.
30 H. Zhang, X. Meng, C. Liu, Y. Wang and R. Xiao, *Fuel Process. Technol.*, 2017, **167**, 484–490.
31 H. Kawamoto, D. Yamamoto, S. Saka and J. Wood, *Sci*, 2008, **54**, 242–246.

32 M. Zhang, Z. Geng and Y. Yu, *Energy Fuels*, 2011, **25**, 2664–2670.

33 M. S. Chambers, D. S. Keeble, D. Fletcher, J. A. Hriljac and Z. Schnepp, *Inorg. Chem.*, 2021, **60**, 7062–7069.

34 Y. Jia and J. Lei, *Energy Explor. Exploit.*, 2023, **41**, 1663–1675.

35 Y. Liu, S. Wu, H. Zhang and R. Xiao, *Fuel Process. Technol.*, 2022, **235**, 107367.

36 L. B. Robinson, W. B. White and R. Roy, *J. Mater. Sci.*, 1966, **1**, 336–345.

37 X. Zhu, F. Qian, Y. Liu, D. Matera, G. Wu, S. Zhang and J. Chen, *Carbon*, 2016, **99**, 338–347.

38 I. Bressler, B. R. Pauw and A. F. Thünemann, *J. Appl. Crystallogr.*, 2015, **48**, 962–969.

39 ISO, *Determination of the Specific Surface Area of Solids by Gas Adsorption. BET Method. ISO 9277*, 2022, pp. 1–21.

40 ISO. *Pore Size Distribution and Porosity of Solid Materials by Mercury Porosimetry and Gas Adsorption – Part 2: Analysis of Nanopores by Gas Adsorption, ISO 15901-2*, 2022, pp. 1–28.